



## Wafer-scale self-assembled plasmonic thin films

Anil Desireddy<sup>a</sup>, Chakra P. Joshi<sup>a</sup>, Michelle Sestak<sup>b,c</sup>, Scott Little<sup>b,c</sup>, Santosh Kumar<sup>a</sup>, Nikolas J. Podraza<sup>b,c</sup>, Sylvain Marsillac<sup>b,c</sup>, Robert W. Collins<sup>b,c</sup>, Terry P. Bigioni<sup>a,c,\*</sup>

<sup>a</sup> Department of Chemistry, The University of Toledo, Toledo, OH 43606, USA

<sup>b</sup> Department of Physics and Astronomy, The University of Toledo, Toledo, OH 43606, USA

<sup>c</sup> Wright Center for Photovoltaics Innovation and Commercialization, The University of Toledo, Toledo, OH 43606, USA

### ARTICLE INFO

#### Article history:

Received 15 October 2010

Received in revised form 17 March 2011

Accepted 22 March 2011

Available online 6 April 2011

#### Keywords:

Plasmon

Monolayer

Nanoparticle

Nanocrystal

Colloid

Self-assembly

Noble metal

Ellipsometry

### ABSTRACT

Plasmonic films have become important for many applications including photonics, energy conversion, and chemical sensing, but the fabrication of these films often requires special equipment, great care, and skill. Colloidal metal nanoparticles offer an alternative as they have been shown to self-assemble into highly-ordered monolayer films by the simple and inexpensive technique of drop casting. Using this technique, we fabricated wafer-scale films of highly-ordered 6 nm Au nanoparticles and evaluated them as candidates for plasmonic applications. These colloidal films were found to support uniform and high-quality plasmon modes over the entire area of the wafer. A combination of microscopy and spectroscopy was used to evaluate and correlate the structural and optical qualities of the films. Electron and atomic force microscopy showed that the nanoscale structure of the films was compact and highly ordered, with few defects or bilayers. Spectroscopic ellipsometry showed that the majority of the film was optically quite uniform with some bilayer patches and voids. These were subsequently confirmed by microscopy. Optical analysis of the thin film showed a prominent plasmon resonance band across the entire wafer. The plasmon frequency was quite insensitive to the presence of voids or bilayers. The width of the plasmon band was more sensitive to bilayers, however, and was found to be as much as 15% wider than in monolayer regions. These results indicate that self-assembled colloidal thin films should be suitable for large-scale plasmonic applications.

© 2011 Elsevier B.V. All rights reserved.

### 1. Introduction

Plasmonic thin films have been found to exhibit an interesting range of properties that depend on the details of their structure and environment, in addition to the shape and composition of the constituent elements [1,2]. For example, perforated metal films have been shown to have plasmonically-enhanced light transmission where the spectrum of transmitted light depends on the periodicity of the holes [3,4]. Nanosphere-lithographed arrays of bare metal nanoparticles support plasmons that are quite sensitive to their dielectric environments [5,6]. Inhomogeneous clusters of colloids have been shown to support plasmons whose frequencies vary greatly depending on the local arrangement of particles [7,8]. The optical properties of colloidal films with particle sizes on the order of optical wavelengths have been investigated [9], as have the DC and microwave properties of smaller metal nanoparticles [10,11]. Little is known about the optical properties of highly-ordered monolayers of plasmonic nanoparticles, however. Herein we describe the detailed structural and optical characterization of a highly-ordered monolayer

of 6 nm diameter dodecanethiol-passivated colloidal nanoparticles, self-assembled onto a 2 in. silicon wafer.

Monolayer self-assembly is generally done on an interface, to break the symmetry of the spherical particles. Solid surfaces are most often used to promote 2D assembly [12]. Spin casting is a common method of assembling nanocrystals onto a substrate [13,14], but with variable results and little control of the mechanism of crystallization. Dip coating has been used to form 2D arrays of large colloids [5,15], but requires careful control of the assembly kinetics. Once the particles assemble onto the substrate, however, the particles can no longer rearrange and order.

Liquid interfaces have been used more successfully for making ordered monolayers [16–18]. Nanoparticles on the water subphase of a Langmuir–Blodgett trough tend to be mobile and form more highly-ordered arrays [19–23]. While this technique can be used to cover large areas that are limited only by the size of the trough, it is a delicate procedure to transfer the monolayer onto a solid substrate without disrupting the long-range order, let alone buckling or tearing the film. The use of a liquid interface for self-assembly was improved upon by Nagayama, who used a convex mercury subphase to nucleate a single domain and produce higher-quality 2D protein crystals [24]. This method was adapted by Andres, who deposited non-polar nanoparticles onto a convex water subphase [21]. Both methods, however, still required transfer to a solid substrate.

\* Corresponding author at: Department of Chemistry, The University of Toledo, 2801 W. Bancroft St., Toledo, Ohio 43606, USA. Tel.: +1 419 530 4095; fax: +1 419 530 4033.  
E-mail address: [Terry.Bigioni@utoledo.edu](mailto:Terry.Bigioni@utoledo.edu) (T.P. Bigioni).

Drop casting nanoparticles onto a solid substrate eliminates the need to transfer the monolayer, but normally produces poorly ordered films [25–30]. This has been attributed to non-equilibrium effects during evaporation, including the kinetics of assembly during the final stages of drying [31–33]. More recently, a drop casting technique was developed that produced highly-ordered monolayers [34]. The basis for this technique is the assembly of nanoparticles at the liquid–air interface of the drop [35,36], rather than on the substrate. This allows the well-solvated nanoparticles time to rearrange into a well-ordered lattice before the monolayer film is deposited onto the solid substrate as the drop finally dries.

Herein we report the fabrication and detailed structural and optical characterization of a highly-ordered, compact monolayer of colloidal Au nanoparticles, self-assembled onto a 2 in. Si wafer. Electron microscopy and spectroscopic ellipsometry were used to evaluate the uniformity and quality of this large-scale film. These complementary techniques provided detailed information about the uniformity of the nanoscale structure and the optical properties of the monolayer film over its entire area. The film was found to support high-quality plasmon modes across the entire wafer. Although two regions were found to deviate somewhat from monolayer coverage, the optical properties of these regions did not differ significantly from the monolayer regions. These results indicate that self-assembled colloidal thin films have robust optical properties that should make them suitable for large-scale plasmonic applications.

## 2. Experimental

### 2.1. Materials

Dimethyldidodecylammonium bromide (DDAB) (99%),  $\text{NaBH}_4$  (99%) and  $\text{AuCl}_3$  (99%) were purchased from Sigma Aldrich. Dodecanethiol (98%) was purchased from Acros Organics. These materials were used without further purification. Toluene was purchased from Fisher and Type 4 molecular sieves were added to remove residual water. Single-side polished 2 in. diameter Si wafers were obtained from Nova Electronic Materials, Inc., with  $\langle 100 \rangle$  orientation and 1–10  $\Omega\text{-cm}$  conductivity.

### 2.2. Au nanocrystal synthesis

All experiments were done following methods described elsewhere [37]. Briefly, 156 mg of DDAB and 52.7 mg of  $\text{AuCl}_3$  were dissolved in 15 mL of dry toluene, with the help of sonication for 15 min. A clear yellow solution was obtained. Next, 54  $\mu\text{L}$  of 9.4 M  $\text{NaBH}_4$  aqueous solution was added drop wise to the solution while stirring at room temperature. The solution slowly darkened to black followed by a deep wine red color. After about 15 min of stirring, 1.2 ml of dodecanethiol was added to the gold colloid and stirred for 1 min. The ligated nanocrystals were then precipitated with ethanol.

Precipitates were separated from the liquid, dried under vacuum, and then redissolved in 15 ml toluene with 1.2 ml of dodecanethiol. This material was refluxed at 110 °C for 3 h to improve the size distribution of the Au nanocrystals [38–40]. After refluxing, the solutions were transferred to a 60 °C water bath and left overnight [38]. The top half of the solutions were carefully separated from the bottom half, as they contained the monodisperse ~6 nm gold nanocrystals.

The monodisperse fraction was precipitated twice with ethanol to clean the particles and to remove as much excess dodecanethiol as possible. The dry precipitate was then redissolved in toluene with a 0.5% volume fraction of dodecanethiol. This solution was centrifuged at 14,000 rpm (16,873 rcf) for 10 min to remove aggregates or other particulates.

### 2.3. UV–vis absorption spectroscopy

Absorption spectra were obtained using a Nicolet Evolution 300 spectrophotometer from Thermo Electron Corporation. Absorption measurements were used to adjust the gold colloid concentration to  $2.0 \times 10^{13}$  nanoparticles/ml, which corresponds to an absorbance of 1.05 at 525 nm. Before measuring the absorbance, solutions were heated for about 10 min to break up any aggregates that may have existed in the solution. Heating generally darkened the solutions.

### 2.4. Monolayer self-assembly

Solutions of ~2000  $\mu\text{L}$  colloidal gold nanocrystals were deposited onto 2 in. diameter Si wafers, which have an area of ~2000  $\text{mm}^2$ . Fresh Si wafers were used without cleaning or surface modification. The solutions were heated before deposition. Covering the entire wafer with a single monolayer required approximately  $4.0 \times 10^{13}$  nanoparticles. The solutions wet the entire surface, pinning at the edges. Airflow was controlled such that crosscurrents were eliminated, and the wafer was kept on a perfectly leveled surface. These conditions were required for a uniform coating.

### 2.5. Optical microscopy

Video microscopy was used to observe the self-assembly of Au nanocrystals on the liquid–air interface. Optical images were captured using an Olympus BX-61 optical microscope with an Olympus DP71 digital camera, capable of 12 MPix still images and 1.4 MPix movies recorded at 25 fps.

### 2.6. Scanning electron microscopy (SEM)

SEM images were acquired on a Hitachi S-4800 using a secondary electron detector and an acceleration voltage of 10–30 kV. Samples were allowed to dry completely, under vacuum if necessary, before being transferred into the SEM chamber for imaging.

### 2.7. Scanning transmission electron microscopy (STEM)

STEM images were acquired on a Hitachi HD-2300A at an operating voltage of 200 kV. Samples were prepared by drying a drop of colloidal nanoparticles on 200 and 400 mesh Cu grids obtained from Pacific Grids Inc. Samples were allowed to dry completely, under vacuum if necessary, before being transferred into the STEM for imaging.

### 2.8. Spectroscopic ellipsometry (SE)

Spectroscopic ellipsometry data were obtained over a 3.3 mm triangular grid covering the area of the sample using a J. A. Woollam Company Accumap-SE system based on the rotating compensator principle [41]. The spectral range of the instrument is 0.75 eV to 6.5 eV. Data were acquired at 127 spots on the sample, with an acquisition time of 8 s/spot and an ellipsometer translation time of approximately 4 s, resulting in a 25 min total scan time. The ellipsometer beam was approximately 2 mm in diameter, and at the angle of incidence of 65°, an elliptical spot on the surface is generated with a major axis 5 mm in length. The scanned area included interior and near-edge locations that were roughly 5 mm away from the edge of the sample. The inability to measure extreme edge points (<2.5 mm from the edge) is due to the ellipsometry beam size.

### 2.9. Atomic force microscopy (AFM)

AFM images were acquired on a Veeco Dimension V AFM. Topographic and phase contrast images were acquired in tapping mode using cantilevers with a force constant of 42 N/m.

### 3. Results and discussion

In order to produce the most uniform monolayer films, several conditions were met. First, the solution of Au nanoparticles wet the entire surface, pinning at the edges. This ensured that depinning did not occur until after the monolayer was completely formed on the liquid–air interface and suppressed the deposition of colloids at the moving contact line [32]. Second, the solution contained slightly more nanoparticles than were needed to cover the wafer with a single monolayer of nanoparticles. Once the monolayer was formed the extra nanoparticles were deposited at the edges of the wafer in the familiar “coffee stain” pattern [31], leaving the interior of the film largely free of bilayers. Third, the wafer was kept flat since inclines cause early depinning on the higher side of the wafer. Fourth, airflows were eliminated since they cause early depinning on the windward side of the wafer. Finally, the solution was cleaned of aggregates and the wafer was protected from exposure to dust, since solid objects protruding high above the substrate can cause local pinning and disrupt monolayer formation and deposition.

In a typical experiment, the solution of Au nanoparticles was deposited onto a wafer that was either sitting on a microscope stage for imaging, as shown in Fig. 1(a), or in a partially open bell jar for control of airflow. In the former case, the liquid–air interface was imaged by video microscopy to ensure that monolayer formation followed the previously identified self-assembly mechanism [35,36]. This was visualized as monolayer islands growing on the liquid–air interface, as shown in Fig. 1(b). The nanoparticle islands eventually merged and the voids filled in to form a continuous monolayer across the entire area of the wafer. After approximately 20 min of evaporation the liquid layer depinned and the self-assembled monolayer film was set down onto the substrate. When the above conditions were met, the resulting monolayer films were visually very uniform in color and contrast, as shown in Fig. 1(c). SEM imaging showed that the self-assembly process produced a compact and ordered nanoparticle array, shown in Fig. 1(d).

Both naked eye observations and optical microscopy showed that the dried nanoparticle films were very uniform over the entire wafer, with the exception of the edges (*vide infra*). These results showed that the interfacial self-assembly mechanism can be used to uniformly coat

much larger areas than previously shown. For example, previous work showed that macroscopically uniform films could be made over  $\sim 10 \text{ mm}^2$  area [36]. In the present study, the substrates were more than 2 orders of magnitude larger with an area of  $\sim 2000 \text{ mm}^2$ . Further, by using entire wafers, the lateral dimensions of the evaporating drop are more than an order of magnitude larger than its vertical dimension. With this separation of scale, it is clear that fluid dynamical effects that depend on the dimensions of the drying drop, such as Rayleigh–Bénard convection, do not play a determinant role in the self-assembly mechanism. Since there is no dependence on the lateral length scale, there should be no upper limit on the area of the films made by this method.

Although previous studies showed this method produces excellent arrays, imaging of nanometer-scale uniformity and order was limited to  $70 \times 70 \mu\text{m}^2$  regions near the center of the substrate. This limitation was due to the use of TEM-transparent  $\text{Si}_3\text{N}_4$  windows that were etched into the center of Si substrates [36,42]. In the present study, the nanoscopic structure of the films was evaluated over the entire wafer, an area that was more than 5 orders of magnitude larger.

SEM imaging showed excellent nanometer-scale uniformity with compact and ordered nanoparticle arrays across the wafer, as shown in Fig. 2. Long-range ordering was generally observed, with a relatively low defect density and very few void spaces. Voids were rare and typically very small, usually point vacancies. Dirt and dust was capable of disrupting the monolayer with large voids and tears, but careful cleaning and environmental controls could eliminate this issue.

The defects observed in the monolayer domains were similar to those found in atomic lattices, including dislocations, point vacancies, and bilayers (cf. adatoms). Unlike atomic lattices, however, the nanoparticle lattices were very tolerant of the strain created by different sizes of particles. This can be attributed to the soft ligand shell around each nanoparticle. Imaging shows that these soft colloidal lattices are capable of redistributing stresses and accommodating nanoparticles that would otherwise be too big or too small to fit in their lattice positions.

Grain boundaries can also be observed in the films. An example is shown in the top center panel of Fig. 2. Grain boundaries generally result from the merging of monolayer islands and are compact, with

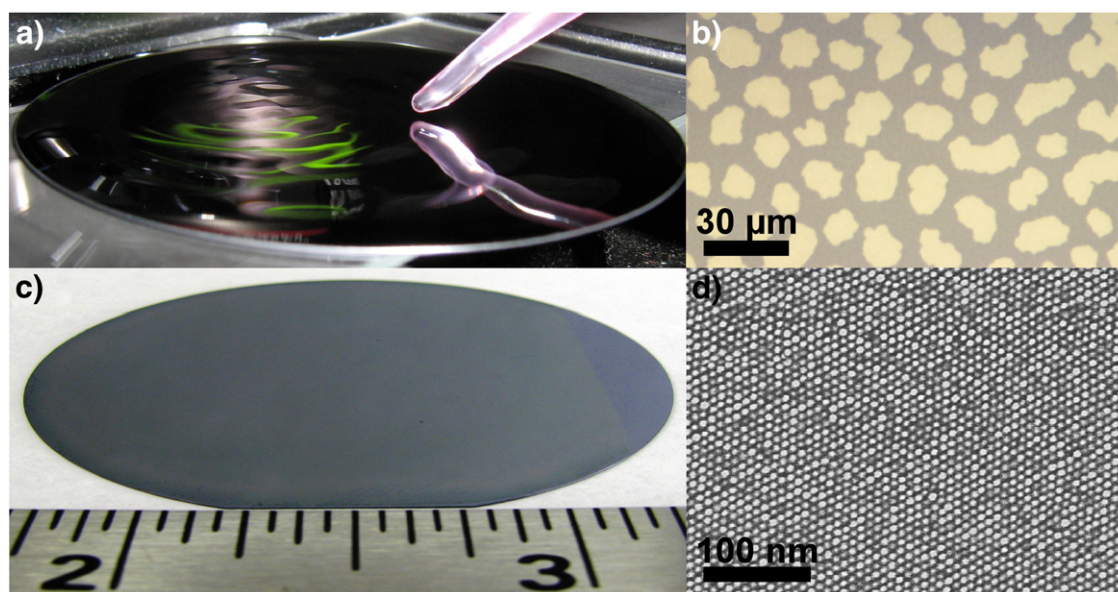


**Fig. 1.** Wafer-scale self-assembly of Au nanocrystals. (a) Deposition of Au solution on a 2 in. Si wafer on the stage of an optical microscope. (b) Optical image of subsequent self-assembly of monolayer islands on the liquid–air interface. (c) Uniform monolayer coating of nanoparticles on wafer in (a), after drying. The right hand side of the wafer was wiped clean to help visualize the 6 nm Au nanoparticle monolayer. (d) SEM image of resultant monolayer showing a compact and ordered array of nanoparticles.

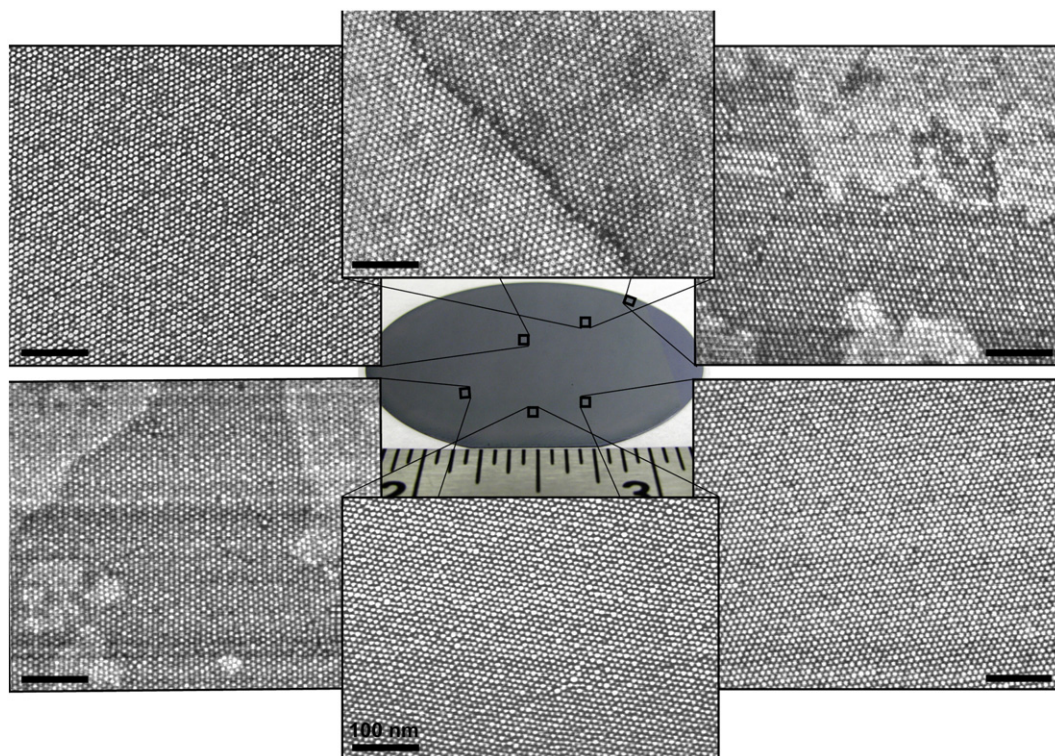


**Fig. 2.** SEM images of the colloidal Au nanoparticles self-assembled onto the 2 in. Si wafer, pictured in the center of the montage. Each SEM image was acquired with secondary electrons and corresponds to a different area on the wafer, as indicated. Most areas are uniform, compact, highly ordered, and only one monolayer thick. Thicker deposits of material are commonly found near the edge of the wafer (upper right). Occasionally small patches of what appear to be bilayers are found (lower left). All scale bars are 100 nm. Locations of images are approximate.

no large voids between domains. Single-crystal domain sizes are related to the island sizes observed in the optical images, such as those shown in Fig. 1(b). As a result, each ellipsometric measurement spanned many grains and grain boundaries.

Although the films showed excellent nanometer-scale uniformity over most of their extent, occasionally there were regions with different contrast. For example, the bottom left panel of Fig. 2 has several brighter regions that appear to be bilayers, which typically consisted of anywhere between one and a few hundred nanoparticles. The rows of nanoparticles generally continued without deviation between the lighter and darker regions, rather than being offset by a half row as expected for hard-sphere stacking. Although the additional signal and contrast could be due to a layer of contaminants

or other material on top of the monolayer film, additional material *underneath* the monolayer is a more likely explanation.

The mechanism of monolayer formation makes it possible to trap nanoparticles below a monolayer sheet. The sheet could drape itself over the trapped particles and still retain its structure and ordering [42,43]. In that case, uninterrupted rows of nanoparticles would be expected with additional contrast provided by the extra layer of Au nanoparticles underneath the monolayer. This would appear as a brighter region in a micrograph, as observed in Fig. 2, due to the additional secondary electrons contributed by the underlayer.

To establish that the contrast mechanism was due to the second layer of nanoparticles, AFM and SEM measurements were used to correlate height and contrast [44]. Both sets of measurements were

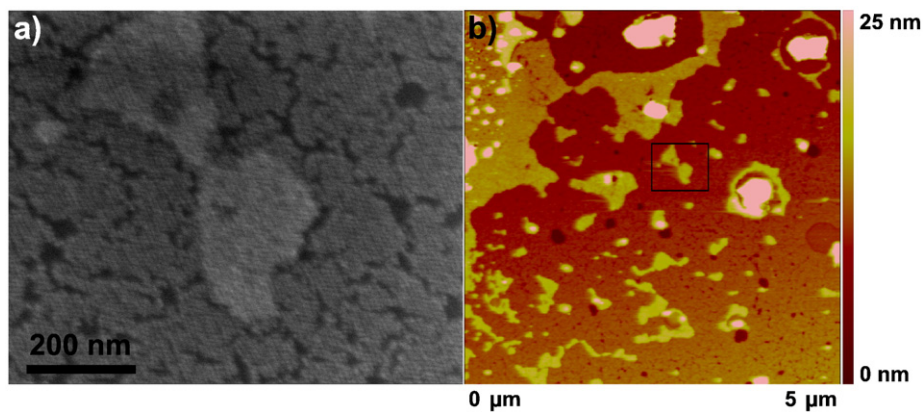


**Fig. 3.** (a) SEM image of a bilayer region on an aged sample. The cracks are consistent with mass loss and contraction of the lattice due to drying. The lattice of the bilayer aligns with that of the surrounding monolayer, as expected for a monolayer that is draped over a group of nanoparticles beneath. (b) AFM image of the same bilayer region, with the area of the SEM image indicated by the box. AFM imaging shows that the contrast in the SEM image corresponds to topographic differences, with the darkest and lightest regions being the substrate and bilayer, respectively. The AFM image is  $5 \times 5 \mu\text{m}^2$ .

made on precisely the same area on the wafer, as shown in Fig. 3, a well-dried sample was used to avoid the complications of excess liquid thiol on imaging. Comparisons of secondary electron imaging with AFM imaging showed that bilayers and voids correlated well with the brightest and darkest contrast, respectively.

The discrete transitions in color and contrast can be interpreted to be single monolayer differences in film thickness. For example, in Fig. 3(a) the darkest regions appear to be holes and cracks in the film while the lightest regions appear to be bilayers. These features correlate very well with the features that are highlighted by the box in the AFM image, in Fig. 3(b). The small dark orange patches appear to be holes while the large yellow patches appear to be bilayers. The bright yellow or white patches would then be multilayer regions.

Height measurements from Fig. 3(b) clearly showed that the changes in contrast corresponded to monolayer and bilayer regions as well as the substrate, validating the above contrast interpretation. The height difference between monolayer and substrate was  $\sim 6.5$  nm. This appears to be too small for ligand-passivated Au nanoparticles with a core diameter of  $\sim 6$  nm. There could be several explanations for this observation, including (i) depletion of the ligand shell from excessive drying, (ii) spreading of the ligand shell to allow the core to approach the substrate [45], and (iii) flattening of the ligand shell to minimize the surface free energy of the ligand–air interface. The height difference between monolayer and bilayer was  $\sim 6.1$  nm, which is consistent with the above effects in addition to nesting in three-fold hollow sites.

It should also be noted that the brightness and contrast of the individual nanoparticles also varied, as seen in Fig. 2. To better understand this, secondary electron images were compared with bright field STEM images since voids, monolayers, and bilayers could easily be differentiated in bright field imaging, as seen in Fig. 4. Different sizes of particles could lead to different contrast, due to mass-thickness contrast in bright field imaging and topographic contrast in secondary imaging, but the size distribution alone could not account for the observations. The most likely source of contrast was the diffraction contrast between darker and lighter regions in Fig. 4(a), due to Bragg scattering of the beam. Interestingly, particles can repeatedly change from dark to light under intense illumination, as if blinking. This is presumably due to momentum transfer from the beam, which could cause the particles to rotate and periodically satisfy the Bragg condition.

Particle size also provided a clear source of contrast, with the largest particles being darkest in transmission imaging and brightest in secondary electron imaging. This is due to the greater ability to block electrons and the greater ease of escape of the secondary electrons, respectively. This was not always true, however. Some of the brighter particles were no bigger than the surrounding particles, as can be clearly seen in Fig. 2. The random distribution of light and dark particles could be related to the crystallography of the metal cores, although the diffraction contrast in Fig. 4(a) did not in general correlate with the brightness of particles in the secondary electron image in Fig. 4(b). Ligand density could also be a source of this seemingly random contrast, but the precise mechanism remains unclear.

Fig. 4 also shows contrast that results from thickness and from excess thiol. Regions containing many layers (upper left of Fig. 4) entirely blocked the beam in transmission, making it impossible to determine thickness. This region appeared especially bright in secondary imaging, but detail from the surface could still be obtained. However, regions were occasionally found where the thickness could be determined because the contrast between several layers changed discontinuously (not shown).

Areas containing excess thiol appeared as bright regions in secondary electron imaging (upper right of Fig. 4(b)). Although it appears similar in contrast to a multilayer patch in the SEM image, only a diffuse dark region appears superimposed over the nanoparticle array in the STEM image (upper right of Fig. 4(a)).

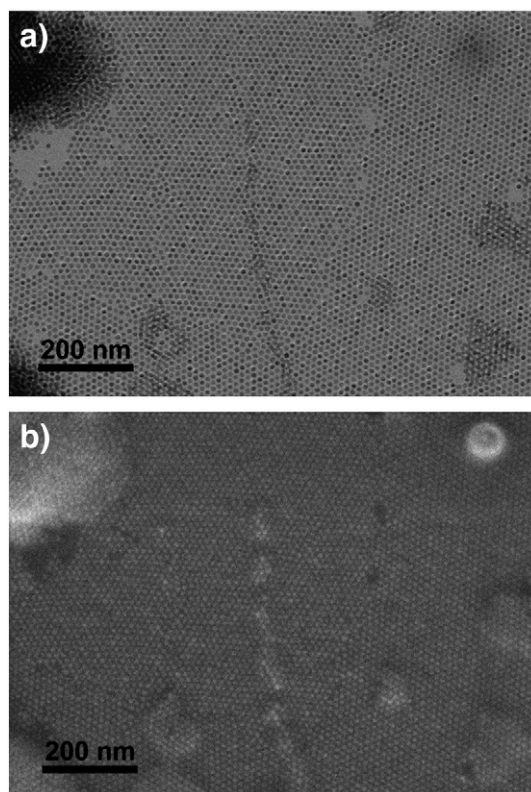


**Fig. 4.** STEM images of a film on a TEM grid using (a) bright field and (b) secondary electron imaging modes, both at 200 kV, showing monolayer, bilayer and void regions. The different contrast of each region can be clearly identified in the bright field image (a) and correlated with the secondary electron image (b). A thick deposit is also visible in the upper left corner of each image, appearing opaque in (a) and bright in (b). Also, the circular bright patch in the upper right hand corner of image (b) appears to be due to excess thiol. This appears as a darkened area in (a).

Cracks were only observed in our monolayer films under certain conditions. Cracks were most commonly observed in aged films, as shown in Fig. 3(a). Cracking typically required a few weeks and appears to be due to mass loss during long term drying [46]. In general, care was taken to measure the spectra of fresh films since such an evolution in structure could change the optical spectra.

In addition to characterizing the film's optical properties, spectroscopic ellipsometry was also used to quantitatively evaluate the macroscopic uniformity of the film across the entire wafer, with sub-nanometer precision in the z-direction. The large size of the ellipsometry beam ( $\sim 2$ – $5$  mm) ensured that each measurement represented an average over the microscopic non-uniformities.

Spectra were taken at 91 interior locations and 36 near-edge locations, and were analyzed using least squares regression and the model shown in Fig. 5. The dielectric functions of the substrate and dielectric layers were extracted from a known database for single-crystal Si and SiO<sub>2</sub>, respectively. The dielectric function of the dodecanethiol in contact with the substrate can also be adequately represented by the SiO<sub>2</sub> dispersion, so the dielectric layer thickness includes a ligand component [47]. The dielectric function of the Au nanoparticle layer was parameterized using three Lorentz oscillators modified with a single band gap to suppress absorption at photon energies below the plasmon band [48].

The results of this analysis showed clear correlations between each of the two best fit thicknesses in Fig. 5 and the quality of the least squares fit, given by the mean square error (MSE) between the measured and best fit calculated ellipsometric spectra  $\psi$  and  $\Delta$ . Here  $\psi$  and  $\Delta$  are defined according to  $r_p/r_s = \tan\psi \exp(i\Delta)$ , where  $r_p$  and  $r_s$  are the complex amplitude reflection coefficients for  $p$  and  $s$  polarized

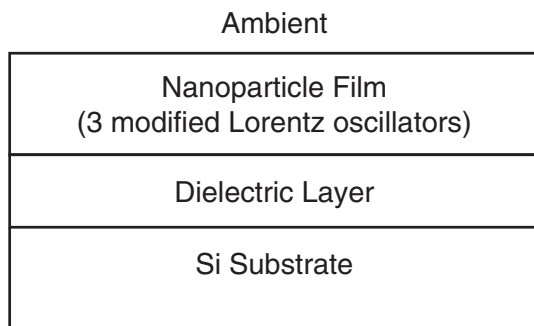


**Fig. 5.** Structural model used for non-linear least-square regression analysis to extract the layer thicknesses and the dielectric functions of the Au nanoparticle layer. The dielectric layer represents both the Si native oxide as well as the non-absorbing dodecanethiol contribution from the nanoparticle film.

light. The minimum MSE was found for a nanoparticle layer thickness of 7.5 nm and a dielectric layer thickness of 4.1 nm. The 7.5 nm thickness is consistent with one monolayer of Au nanoparticles, with 6 nm associated with the nanoparticle itself and 1.5 nm associated with the ligands [47]. The 4.1 nm dielectric layer can then be attributed to 2.6 nm of native oxide on the Si substrate and 1.5 nm of ligands. Based on this interpretation, the increase in MSE with nanoparticle layer thickness below and above the minimum value can be attributed to observable deviations of the layer structure from a single perfect monolayer which is described optically by the Fresnel equations for reflection and transmission.

In order to proceed systematically, the  $\psi$  and  $\Delta$  spectra for the lowest MSE point were mathematically inverted to extract the real and imaginary parts of the dielectric function  $\epsilon_1$  and  $\epsilon_2$  of the nanoparticle layer of Fig. 5, using the thicknesses of the two layers as fixed parameters (7.5 nm and 4.1 nm). Then this dielectric function and the underlying dielectric layer thickness were fixed in a further analysis of the nanoparticle layer thickness. This approach is based on the supposition that the differences in structure that give rise to the differences in MSE are reflected primarily in the fact that some measured spots cover regions with void spaces in a single monolayer whereas other spots cover regions with bilayers.

The resulting map of nanoparticle layer thickness generated with this sequence of analysis steps is shown in Fig. 6. This map shows a relatively large central region of average thickness  $7.5 \pm 0.7$  nm. Circular arcs exhibit larger thicknesses with the maximum reaching nearly 11 nm, consistent with the existence of bilayer regions within the probed spot.

The variation of thickness shown in Fig. 6 can be interpreted as the variation in the fraction  $f$  of bilayer that was covering the probed area.

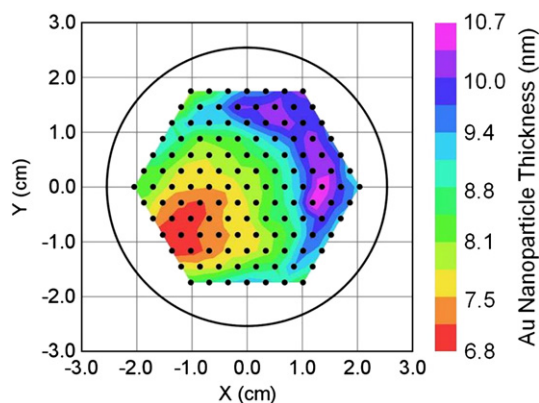


**Fig. 6.** Map of Au nanoparticle thickness in nm over the entire area of the wafer, obtained using the model of Fig. 5 with fixed dielectric layer and fixed nanoparticle film dielectric function. The wafer was oriented such that the flat was at the bottom.

One can estimate this area fraction  $f$  directly from the thickness according to a simple linear interpolation:  $f = (d/d_{ML}) - 1$ , where  $d$  is the measured thickness and  $d_{ML}$  is the thickness of a monolayer. This interpolation holds due to the linearity between the measured data (Fourier coefficients of the irradiance waveform) and the thickness for such thin layers. Note that this fractional measurement is due to the averaging of monolayer and bilayer thicknesses over the footprint of the beam. Other interpretations of the observed  $\sim 11$  nm thickness are possible, for example, additional material underneath the nanoparticle film.

Thus, imaging was done to follow up and validate the interpretation of the ellipsometry data. SEM imaging in the thickest (violet) area in Fig. 6 confirmed the existence of bilayer patches in this region. Most patches were a few tens to a few hundred nanometers wide. Bilayers as wide as a micron, small trilayer patches, and bilayer coverages as high as  $\sim 0.5$  were observed, although each was rare. Large areas of only monolayer coverage were also found in this area, however, as seen in Fig. 2 (top center panel).

SEM imaging in the thinnest (red) area in Fig. 6 showed that this region contained voids. These voids were typically only a few particles in size but could be as large as a few tens of nanometers, with the largest observed being  $\sim 200$  nm wide. The largest observed void area fraction was  $\sim 0.1$ , though it was typically far lower. Interestingly, this area also contained a few bilayer patches.

This subtle variation in film quality correlates with the observed drying pattern. Although the liquid depinned uniformly from the perimeter of the wafer, the subsequent drying was asymmetric. Namely, the contact line moved toward the center of the wafer more rapidly from the bottom left edge than it did from the top right edge, using the same wafer orientation as in Fig. 6. Consequently, the center of mass of the remaining liquid drop did not stay at the center of the wafer. Rather, it moved toward the upper right edge of the wafer such that the final area to dry was in the vicinity of the thickest (violet) area in Fig. 6. The natural consequence of the above drying pattern would be the deposition of additional material in the area that was last to dry.

These results indicate that, if required, the uniformity of the films could be further improved by controlling depinning and dewetting during the final stages of drying. Further, given an optical model verified by direct imaging, the mapping spectroscopic ellipsometry could be used to provide a rapid, non-invasive means for characterizing the uniformity of the plasmonic films.

In addition to the layer thickness in Fig. 6, the dielectric function extracted by inversion shown in Fig. 7 (points) is of great interest. The broken lines shown in Fig. 7 represent the dielectric function of bulk Au. From this result, one can identify the origin of the three oscillators required in the analytical model. One oscillator near 2.1 eV corresponds to the plasmon resonance. This prominent and sharp absorption band is due to the nanoparticles in the array, and is not present in bulk Au. The other two oscillators at higher energies are associated with the interband resonances of bulk Au.

The solid line in Fig. 7 represents the best fit analytical result based on the three oscillator model. It is apparent that the analytical description of the dielectric function matches the inverted result quite closely. As a result, an analysis that uses a variable dielectric function in the form of an analytical model with photon-energy independent oscillator parameters enables accurate identification of the plasmon peak position. The resulting map is shown in Fig. 8. Excluding an upper left edge point, all values on this map lie within the range of  $2.142 \pm 0.014$  eV, or a  $\pm 0.6\%$  variation. This variation is correlated with the drying pattern, suggesting a slightly higher resonance energy in the bilayer region. The more dominant effect is in the Lorentzian broadening energy of the plasmon band, shown in Fig. 9. This energy increases from 0.40 to 0.47 eV (excluding near-edge points) from the monolayer to the bilayer region. This increase in width, by 15%, is likely due to a shorter plasmon relaxation time associated with the nanoparticles in the bilayer.

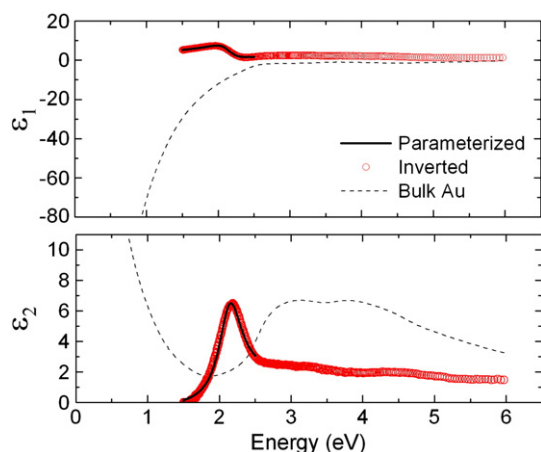


**Fig. 7.** Inverted (points) and parameterized (lines) real (top) and imaginary (bottom) parts of the dielectric function for the Au nanoparticle film, using the region of the wafer where the thickness was  $\sim 1$  monolayer. Also shown is the bulk Au dielectric function for reference.

It is worth noting that the position of the plasmon resonance is red shifted from that of the solution ( $\sim 2.35$  eV). This is due to dipole coupling between neighboring particles in the film [5,49,50]. It is also worth noting that for some applications it may be necessary to remove the ligands, which can be done by oxygen or argon plasma etching [51,52]. Removal of the ligands would blue-shift the absorbance band due to the lower dielectric medium surrounding the particles [5].

While the consistency of the optical properties is remarkable, the film quality at the edge of the film differed greatly from that of the interior. The perimeter of the wafer generally did not display the same macroscopic uniformity as the interior of the film, and instead consisted of a multilayer region. This is consistent with colloidal drop drying [31]. In general, advective flows transport material to the edge of an evaporating drop, concentrating the solids around the perimeter. This mechanism forms the familiar “coffee stain” once dried [31].

#### 4. Conclusions

We have demonstrated that the structural and optical properties of these self-assembled plasmonic films are of high quality and can be fabricated over areas large enough to be technologically important. Notably, our optical measurements indicate that the films need not be structurally perfect to be optically uniform. Nanometer-scale SEM images revealed highly-ordered monolayers across the entire wafer, with very few holes and bilayer domains. Spectroscopic ellipsometry revealed some variations in thickness, which were attributed to a

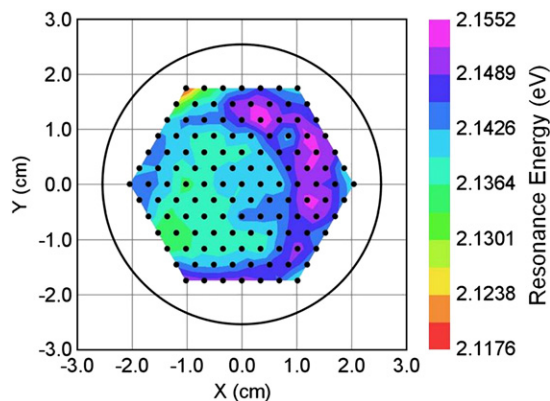


**Fig. 8.** Map of plasmon resonance energy over the entire area of the wafer, obtained using the model of Fig. 5. The wafer was oriented such that the flat was at the bottom.

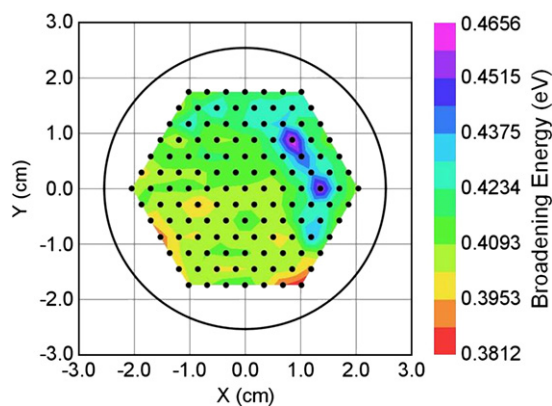


**Fig. 9.** Map of plasmon Lorentzian broadening over the entire area of the wafer, obtained using the model of Fig. 5. The wafer was oriented such that the flat was at the bottom.

drying pattern. Optical analysis also showed that the film had a strong plasmon resonance whose position was insensitive to imperfections in the film. Holes and bilayer patches caused the peak position to vary by only  $\pm 0.6\%$  and the peak width to vary by only about 15%. These results indicate that self-assembled plasmonic thin films of colloidal nanoparticles can be made with high-enough quality and over large enough areas to be suitable for large-scale applications.

#### Acknowledgements

We thank the Center for Photovoltaics Innovation and Commercialization (PVIC) for funding. This work was also partially supported by NSF grant CBET-0955148.

#### References

- [1] U. Kreibitz, M. Vollmer, *Optical Properties of Metal Clusters*, Springer-Verlag, Berlin, 1995.
- [2] K.L. Kelly, E. Coronado, L.L. Zhao, G.C. Schatz, *J. Phys. Chem. B* 107 (2003) 668.
- [3] J. Dintinger, A. Degiron, T.W. Ebbesen, *MRS Bull.* 30 (2005) 381.
- [4] J. Henzie, M.H. Lee, T.W. Odom, *Nat. Nanotechnol.* 2 (2007) 549.
- [5] C.L. Haynes, R.P. Van Duyne, *J. Phys. Chem. B* 105 (2001) 5599.
- [6] X.Y. Zhang, C.R. Yonzon, R.P. Van Duyne, *J. Mater. Res.* 21 (2006) 1083.
- [7] D.P. Tsai, J. Kovacs, Z. Wang, M. Moskovits, V.M. Shalae, J.S. Suh, R. Botet, *Phys. Rev. Lett.* 72 (1994) 4149.
- [8] V.A. Markel, V.M. Shalae, P. Zhang, W. Huynh, L. Tay, T.L. Haslett, M. Moskovits, *Phys. Rev. B* 59 (1999) 10903.
- [9] A. Tao, P. Sinsermsuksakul, P. Yang, *Nat. Nanotechnol.* 2 (2007) 435.
- [10] C.P. Collier, R.J. Saykally, J.J. Shiang, S.E. Henrichs, J.R. Heath, *Science* 277 (1997) 1978.
- [11] G. Markovich, C.P. Collier, J.R. Heath, *Phys. Rev. Lett.* 80 (1998) 3807.
- [12] S. Kinge, M. Crego-Calama, D.N. Reinhoudt, *Chemphyschem* 9 (2008) 20.
- [13] P. Moriarty, M.D.R. Taylor, M. Brust, *Phys. Rev. Lett.* 89 (2002) 248303.
- [14] R.P. Andres, J.D. Bielefeld, J.I. Henderson, D.B. Janes, V.R. Kolagunta, C.P. Kubiak, W. Mahoney, R.G. Osifchin, *Science* 273 (1996) 1690.
- [15] C.L. Haynes, A.D. McFarland, M.T. Smith, J.C. Hulteen, R.P. Van Duyne, *J. Phys. Chem. B* 106 (2002) 1898.
- [16] Y. Lin, H. Skaff, T. Emrick, A.D. Dinsmore, T.P. Russell, *Science* 299 (2003) 226.
- [17] A.D. Dinsmore, M.F. Hsu, M.G. Nikolaidis, M. Marquez, A.R. Bausch, D.A. Weitz, *Science* 298 (2002) 1006.
- [18] M.N. Martin, J.I. Basham, P. Chando, S.K. Eah, *Langmuir* 26 (2010) 7410.
- [19] B.O. Dabbousi, C.B. Murray, M.F. Rubner, M.G. Bawendi, *Chem. Mater.* 6 (1994) 216.
- [20] G. Markovich, C.P. Collier, S.E. Henrichs, F. Remacle, R.D. Levine, J.R. Heath, *Acc. Chem. Res.* 32 (1999) 415.
- [21] V. Santhanam, J. Liu, R. Agarwal, R.P. Andres, *Langmuir* 19 (2003) 7881.
- [22] W.Y. Lee, M.J. Hostetler, R.W. Murray, M. Majda, *Isr. J. Chem.* 37 (1997) 213.
- [23] J.R. Heath, C.M. Knobler, D.V. Leff, *J. Phys. Chem. B* 101 (1997) 189.
- [24] M. Yamaki, K. Matsubara, K. Nagayama, *Langmuir* 9 (1993) 3154.
- [25] L. Motte, F. Billoudet, E. Lacaze, J. Douin, M.P. Pileni, *J. Phys. Chem. B* 101 (1997) 138.
- [26] C. Petit, A. Taleb, M.P. Pileni, *J. Phys. Chem. B* 103 (1999) 1805.
- [27] G.L. Ge, L. Brus, *J. Phys. Chem. B* 104 (2000) 9573.
- [28] C. Stowell, B.A. Korgel, *Nano Lett.* 1 (2001) 595.
- [29] C.J. Kiely, J. Fink, M. Brust, D. Bethell, D.J. Schiffrin, *Nature* 396 (1998) 444.
- [30] B.A. Korgel, D. Fitzmaurice, *Phys. Rev. Lett.* 80 (1998) 3531.
- [31] R.D. Deegan, O. Bakajin, T.F. Dupont, G. Huber, S.R. Nagel, T.A. Witten, *Nature* 389 (1997) 827.

- [32] R.D. Deegan, Phys. Rev. E 61 (2000) 475.
- [33] E. Rabani, D.R. Reichman, P.L. Geissler, L.E. Brus, Nature 426 (2003) 271.
- [34] X.M. Lin, H.M. Jaeger, C.M. Sorensen, K.J. Klabunde, J. Phys. Chem. B 105 (2001) 3353.
- [35] S. Narayanan, J. Wang, X.-M. Lin, Phys. Rev. Lett. 93 (2004) 135503.
- [36] T.P. Bigioni, X.M. Lin, T.T. Nguyen, E.I. Corwin, T.A. Witten, H.M. Jaeger, Nat. Mater. 5 (2006) 265.
- [37] X.M. Lin, C.M. Sorensen, K.J. Klabunde, J. Nanopart. Res. 2 (2000) 157.
- [38] X.M. Lin, G.M. Wang, C.M. Sorensen, K.J. Klabunde, J. Phys. Chem. B 103 (1999) 5488.
- [39] X.M. Lin, C.M. Sorensen, K.J. Klabunde, Chem. Mater. 11 (1999) 198.
- [40] S. Stoeva, K.J. Klabunde, C.M. Sorensen, I. Dragieva, J. Am. Chem. Soc. 124 (2002) 2305.
- [41] J. Lee, P.I. Rovira, I. An, R.W. Collins, Rev. Sci. Instrum. 69 (1998) 1800.
- [42] R. Parthasarathy, X.M. Lin, H.M. Jaeger, Phys. Rev. Lett. 8718 (2001).
- [43] K.E. Mueggenburg, X.M. Lin, R.H. Goldsmith, H. Jaeger, Nat. Mater. 6 (2007) 656.
- [44] K.C. Grabar, K.R. Brown, C.D. Keating, S.J. Stranick, S.-L. Tang, M.J. Natan, Anal. Chem. 69 (1997) 471.
- [45] W.D. Luedtke, U. Landman, J. Phys. Chem. 100 (1996) 13323.
- [46] B.S. Kim, L. Avila, L.E. Brus, I.P. Herman, App. Phys. Lett. 76 (2000) 3715.
- [47] J. Shi, B. Hong, A.N. Parikh, R.W. Collins, D.L. Allara, Chem. Phys. Lett. 246 (1995) 90.
- [48] A.S. Ferlauto, G.M. Ferreira, J.M. Pearce, C.R. Wronski, R.W. Collins, X. Deng, G. Ganguly, J. Appl. Phys. 92 (2002) 2424.
- [49] M.K. Kinnan, G. Chumanov, J. Phys. Chem. B 114 (2010) 7496.
- [50] M. Brust, D. Bethell, C.J. Kiely, D.J. Schiffrin, Langmuir 14 (1998) 5425.
- [51] P. Negri, N.E. Marotta, L.A. Bottomley, R.A. Dluhy, Appl. Spectrosc. 65 (2011) 66.
- [52] J.P. Spatz, S. Mossmer, C. Hartmann, M. Moller, T. Herzog, M. Krieger, H.G. Boyen, P. Ziemann, B. Kabius, Langmuir 16 (2000) 407.